Direct Probing of Fe_3O_4 Nanoparticle Surface Temperatures During Magnetic Heating: Implications for Induction Catalysis

Natalia da Silva Moura, Khashayar R. Bajgiran, Adam T. Melvin, Kerry M. Dooley, James A. Dorman[*]

Department of Chemical Engineering, Louisiana State University, 3307 Patrick F. Taylor Hall, Baton Rouge, LA 70803

KEYWORDS: Induction Heating, Surface Temperature, Colloidal Nanoparticles

The presence of a temperature gradient between the magnetic nanoparticle (NP) surface and the bulk medium during induction heating has been observed across several fields. While no noticeable rise in bulk temperature is observed, biological (DNA denaturation, tumor apoptosis) and chemical (bond cleavage) evidence indicates high temperatures near/at the NP surface. Unfortunately, current methods for temperature probing rely on bulk temperature measurements (fiber optic IR probes) or are limited by thermal stability and spatial resolution (organic molecules). To further the understanding of magnetic heating as a driving force in catalysis, as well as drug delivery/hyperthermia treatments, a more accurate description of the nanoparticle surface temperature is needed. This work uses inorganic luminescent probes in direct contact with the particle surface, entailing the deposition of $YVO_4:Eu^{3+}$ around a $Fe_3O_4|SiO_2$ structure, to measure the local temperature. The luminescent response is calibrated *in situ* via a controlled temperature stage to extract the field dependent heating. The luminescent probe results in high spatial resolution (<5.5 nm) with temperatures up to 64 °C higher than standard fiber optic probes. The direct contact between the PL probe and Fe_3O_4 allows for ballistic transport and improved temporal resolution, mimicking an adiabatic system (negligible long-range heat dissipation). Other advantages include avoiding measurements in liquid media, where the distance between the heat source and the probe cannot be controlled, adding to the uncertainty of the temperature measurement due to changes in colloidal anisotropy (heating profile) of the magnetic cores and surface quenching of the luminescent signal.

INTRODUCTION

In situ heating with magnetic nanoparticles (NP) are now ubiquitous in applications such as induction heating catalysis[1-5], thermo-activated drug delivery[6-7], magnetic fluid hyperthermia[8-9], and water treatment[10]. These technologies represent remarkable advances in nanotechnology and energy efficiency, which benefit from fast heating and cooling, local heating without raising the temperature of the surroundings substantially[11], and process safety[12]. However, to optimize heating processes with magnetic NPs via induction heating, a more detailed understanding of heat propagation at the nanoscale and an accurate determination of the NP surface temperature are still needed. Current studies face experimental limitations regarding spatial and temporal resolution[13], and theoretical models are still unable to predict temperatures accurately given the complexity of heat dissipation at the nanoscale.[6, 14] Predicting heat transport would require expensive calculations to solve the Boltzmann equation with the phonon dispersion relation and rate of collisions. However, the evaluation of the collision term is not trivial, involving multiple calculation steps.[15]

Moreover, current correlations between heat generation (in terms of Specific Loss Power (SLP)) and temperature using classical physics tend to compare the measured medium (bulk) temperatures to calculated values obtained from Fourier's Law[16] and Linear Response Theory[17-18], which are commonly discussed in the field of magnetic hyperthermia applications.[19] The limitations of this approach are that heat transfer treatment is primarily diffusive[20], SLP correlations are only valid when performed under adiabatic conditions[6], and the heat generation is only linear and proportional to the applied magnetic field for small NP diameter (<20 nm).[21] When the magnetic NPs are larger (> 20 nm), heat dissipation is best described by the Stoner-Wohlfarth model (ferro- and ferrimagnetic regimes), and the response is no longer linear.[17] Given the complex relationship between the NP structure and the resultant magnetic properties, a more direct temperature probing method will allow unambiguous comparison across literature works. For instance, NPs of larger size, higher anisotropy[22-23], or in a viscous media will require larger applied fields to exhibit heat dissipation, and some SLP equations include the applied field on their calculation[24], resulting in higher values. Therefore, when comparing the SLP values of different structures of distinct compositions, it is nearly impossible to know the highest performing NPs unless they are all done at the same time by the same research group.

Furthermore, in applications such as catalysis[1-2] the temperature near the NP surface is more important than the temperature of the medium, especially when physical contact is necessary. Catalysis applications are also studied under higher temperatures (>150 °C), where fiber optic probes are no longer reliable, which highlights the importance of alternative probing methods. In these cases, ballistic heat transfer takes place where Fourier's law is no longer applicable for predicting heat dissipation.[25] These factors have contributed to the obstacles of modeling heat transfer at the nanoscale, and experimental probes have provided the best temperature estimates so far.[13]

One experimental approach to temperature resolution was demonstrated by Riedinger et al.[6] using fluoresceineamine (FA) dye attached to polyethylene glycol surfactants on the Fe_3O_4 NPs. The presence of a temperature gradient within 0.5 nm of the NP surface was observed, with the global temperature (bulk) significantly differing from the calculated surface temperature. This was also observed by Creixell et al.[11] when cancer cells were killed (> 43 °C) without an increase in the medium temperature. Unfortunately, molecular probes are not ideal for high-temperature probing due thermal degradation which are not observed with solid luminescent hosts. Additionally, molecular probes add to the interfacial heat transfer resistance and impact the magnetic heating dynamics due to colloidal anisotropy in solution.[17] Improved temperature resolution was demonstrated by Zink et al.[26] utilizing magnetic NPs encapsulated in mesoporous silica and coupled with an upconversion NP (UCNS) luminescent probes, quantifying the temperature within ~8 nm of the NP surface. Using this method, the group observed temperature gradients of ~23 °C from bulk to NPs. Additionally, Pinol et al.[13] also used molecular luminescent probes to show that even infrared cameras lack the necessary surface/temperature resolution, measuring values similar to bulk fiber optic probes. Comparatively, solid luminescent materials have advantages over molecular dyes and thermosensitive polymers because of their higher operational range (>600 K) without probe degradation, reduced parasitic vibrations[27], experimental variations[26], or photobleaching.[28] Specifically, YVO_4 is a commonly used photoluminescent host that is thermally stable, highly transparent in the visible range, non-hygroscopic, and when doped with europium (Eu^{3+}), achieves the highest operating range before luminescence quenching compared to other lanthanide-doped YVO_4.[29] Therefore, to further our understanding of heat propagation at the nanoscale, $YVO_4:Eu^{3+}$ thermometry is chosen to address spatial resolution challenges where infrared cameras, magnetic ferrofluids, and molecular probes have been limited.

This work addresses the issue of temperature resolution for larger NP (> 20 nm) structures, in powder form, and in a temperature range that cannot be accurately determined by thermally labile probes. By focusing on larger structures, high thermal gradients between surface and bulk can be exposed as a foundation for future sensing technologies for applications at lower temperatures (45 °C), where even greater resolution would be required. The multi-layer structure studied in this work allowed temperature probing to ~5 nm spatial resolution from the Fe_3O_4 surface to the luminescent host. Iron oxide (Fe_3O_4) NPs, synthesized via colloidal routes, are encapsulated with a thin SiO_2 passivation layer followed by $YVO_4:Eu^{3+}$, taking advantage of the thermal stability, steady luminescence, sharp $^5D_0$-$^7F_2$ emission band[30-31], and temporal response to changes in temperature (no time delay).[13] Additionally, the SiO_2 layer is expected to aid in the mitigation of luminescence quenching by limiting energy transfer into the Fe_3O_4 or direct UV absorption[32], consequently reducing quenching and improving signal-to-noise ratio.[33] A discussion of heat transfer at the nanoscale is also provided to demonstrate the advantages and disadvantages of this method. All measurements are performed *in situ* and in powder form, with the same sample being previously calibrated in a temperature-controlled stage, where luminescence is measured at various temperatures. Therefore, the correlation of intensity and temperature is compared to the observed intensity at several alternating magnetic fields (AMFs), allowing direct surface temperature measurements due to the close contact between the magnetic and luminescent structures. Such a thermometry strategy has the potential to improve applications with induction heating in catalysis, magnetic hyperthermia, and other biomedical applications, where lower apparent temperatures can be used to drive chemical transformations/heat transfer.

RESULTS AND DISCUSSION

Spherical iron oxide (Fe_3O_4) NPs are synthesized via thermal decomposition (see Methods) to control NP size and monodispersity to maximize the heat generation.[34] The Fe_3O_4 magnetite phase is known to readily oxidize to a less magnetic oxide phase (γ-Fe_2O_3)[35] at low temperatures. Therefore, to prevent this phase transition, the NPs are encapsulated with an SiO_2 layer to limit oxidation/leaching[26], while reducing heat dissipation to the surrounding environemts.[26, 36] The $YVO_4:Eu^{3+}$ structure is then deposited around the SiO_2 encapsulated Fe_3O_4, as shown in Figure 1. The utilization of surfactants for every deposition step (Igepal CO-520 and citric acid for SiO_2 and $YVO_4:Eu^{3+}$, respectively) allows for a more targeted layer deposition. Figure 2a shows the as-synthesized Fe_3O_4, and Figure S1a shows the core NPs encapsulated with SiO_2. The NP diameter, estimated from TEM micrographs, is of 28.8 ± 2.7 nm and increases to 39.8 ± 3.8 nm upon SiO_2 shell deposition or roughly a ~ 5.5 nm semi-conformal shell. Such distance dictates the extent of heat dissipation before the temperature rise can be detected by the luminescent probe (spatial resolution) and is expected to lower the discrepancy between bulk and nano-resolved measurements.[6]

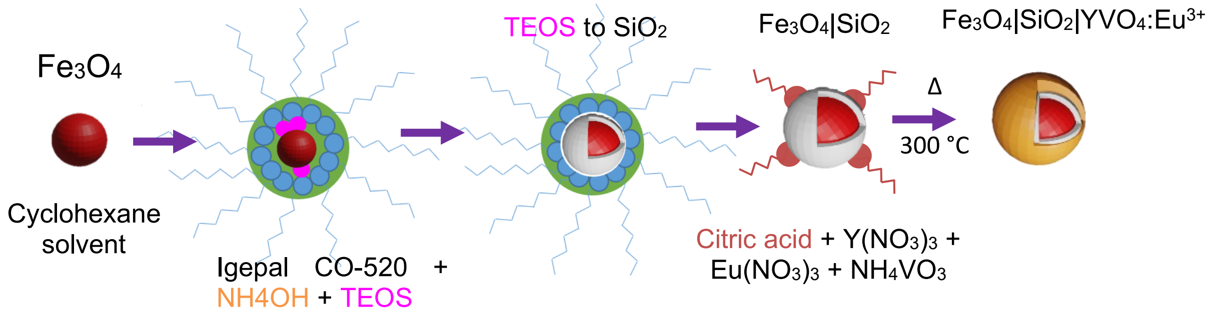

Figure 1: Schematic illustration of the synthesis of a multi-layered $Fe_3O_4|SiO_2|YVO_4$ structure via reverse microemultion (SiO_2 deposition) and sol-gel ($YVO_4:Eu^{3+}$ deposition).

Next, $YVO_4:Eu^{3+}$ (5 mol%) crystals were nucleated on the SiO_2 encapsulated Fe_3O_4 NPs and annealed at 300 °C for 45 min to reduce potential oxidation of the Fe_3O_4 core (Figure S1b). Annealing the samples demonstrated a significant improvement in luminescent signal (Figure S2), enhancing signal-to-noise ratio by a factor of 1.6 without impacting the crystal phase of Fe_3O_4 (Figure 2b). Given the thin theoretical thickness for the $YVO_4:Eu^{3+}$ layer (<10 nm), its crystal phase could not be detected with XRD (Figure 2b); however, lattice spacing measurements with HRTEM enabled crystal phase identification. As shown in Figure 2c, the core NP phase is assigned to the cubic magnetite (ICDD:04-005-4319) after measuring the lattice spacing for the (111) plane. Similarly, the tetragonal vanadate phase (YVO_4, ICSD:174549) is identified based on the (211) plane (d = 2.84 Å). As an additional confirmation for the $YVO_4:Eu^{3+}$ deposition, ICP-OES measurements resulted in a 0.15 Fe/Y wt ratio, which is in agreement with the initial precursor ratios with a ~50% $YVO_4:Eu^{3+}$ reaction yield. Finally, the PL temperature dependency of the

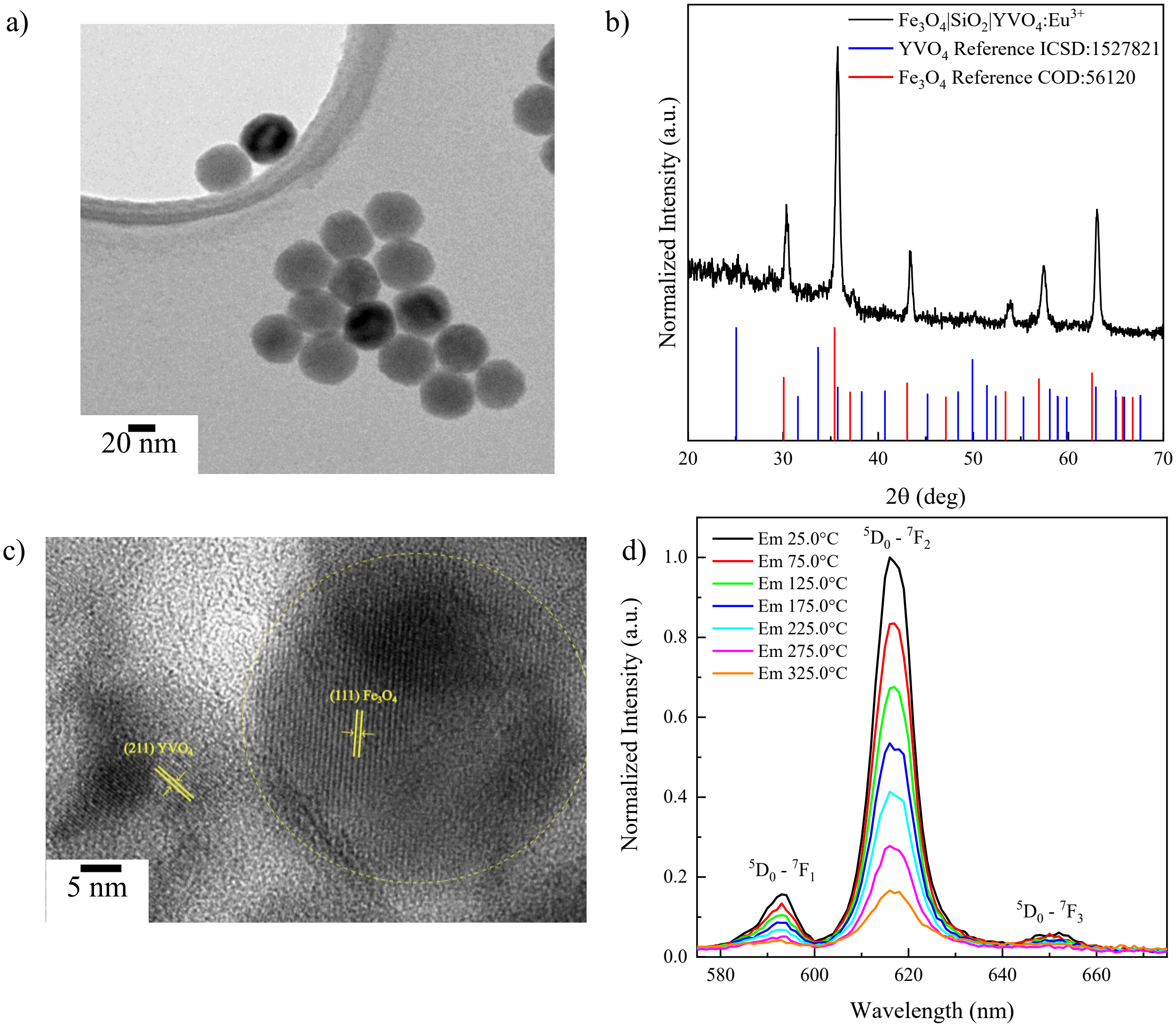

Figure 2: a) TEM for a 28 nm Fe_3O_4 core as-synthesized, b) XRD data shows overlap between the main peaks of Fe_3O_4 abd YVO_4 crystal phases, making it difficult to detect the luminescent phase with a bulk method. However, no changes in the Fe_3O_4 crystal structure are observed after the sample annealing steps. c) HRTEM showing close proximity and lattice spacing identification for Fe_3O_4 and YVO_4. d) PL spectra showing the temperature dependance luminescence intensity for a multi-layered sample.

multilayered NPs was measured in a controlled temperature stage for the multi-layered sample to calibrate the luminescence intensity dependence on temperature (Figure 2d). The emission peak at 618 nm for the $^5D_0 \rightarrow {}^7F_2$ transition of Eu^{3+} is used as the temperature-dependent calibration peak, showing a linear decrease in intensity with increasing temperatures, as expected. Therefore, structural characterization of the multilayered $Fe_3O_4|SiO_2|YVO_4:Eu^{3+}$ NPs indicates close proximity between the heat source and the luminescent probe, which was optimized through the conformality and thickness of the SiO_2 encapsulation. These structures demonstrate a direct relationship between luminescence signal and sample temperature, specifically the Fe_3O_4 surface due to the nature of the hyperthermal heating. Additionally, it is expected that heat dissipation losses are reduced since the short distance between the surface and the luminescent result in faster thermal equilibrium[37] to improve measurement accuracy.

Photoluminescent spectroscopy (PL) measurements under various temperatures and AMFs were carried out and compared to fiber optic temperature readings. The fundamentals of thermal responsive luminescence are based on the Boltzman distribution of electrons between energy levels.[29] As the temperature increases, phonon vibrations bridge excited states which lead to luminescent quenching via non-radiative transitions. The non-radiative transition rate (and the temperature) is proportional to the luminescent lifetime and intensity, providing a direct non-invasive probe to measure the surface temperature.[38] To determine the ability of the luminescent material to quantify the local temperature, four control samples were studied: 1) pristine $YVO_4:Eu^{3+}$ powders, 2) $YVO_4:Eu^{3+}$ mixed with Fe_3O_4 (1.43 wt ratio $YVO_4:Fe_3O_4$), 3) $YVO_4:Eu^{3+}$ mixed core-shell $Fe_3O_4|SiO_2$ (1.43 wt ratio), and 4) $YVO_4:Eu^{3+}$ mixed core-shell $Fe_3O_4|SiO_2$ (2.51 wt ratio). It is expected that the $Fe_3O_4|SiO_2$ will result in lower temperatures than the uncoated Fe_3O_4 due to the SiO_2 poor thermal conductivity. The changes in wt ratio are studied to verify that the luminescent probe can sense the known trend of increased heat generation with the amount of Fe_3O_4 ratio.[21, 39] Figure S3 shows the PL spectra for the $YVO_4:Eu^{3+}$ NPs under various AMF on the luminescence intensity. The Eu^{3+} $^5D_0 \rightarrow {}^7F_2$ emission transition exhibits suppressed PL intensity and peak splitting due to the Zeeman effect (magnetic field dependence), making the luminescence collection under AMF complex.[40] Instead, PL measurements are collected immediately after removing the AMF to negate any field dependence luminescence and limit heat dissipation. There is a negligible effect on the luminescent signal for the pristine $YVO_4:Eu^{3+}$ NPs, decreasing <5% with maximum field strengths (27 mT). The observed variations are attributed to energy level splitting of the unpaired electrons in Eu^{3+} causing minor changes in the YVO_4 symmetry[40] and are not expected to impact the temperature-dependent measurements.

In contrast, the variation in luminescence intensity for the physically mixed samples was significantly higher than the pure $YVO_4:Eu^{3+}$ sample (Figure 3). Specifically, the PL signal decreased by 9%, 15%, and 16% with AMFs up to 27 mT for $YVO_4:Eu^{3+}$ mixed with core-shell $Fe_3O_4|SiO_2$ (2.51 wt ratio, Figure 3a), $Fe_3O_4|SiO_2$ (1.43 wt ratio, Figure 3b), and only the core Fe_3O_4 (1.43 wt ratio, Figure 3c), respectively. These results indicate that less heat is generated with higher concentrations of YVO_4, as expected. Secondly, the inclusion of a thin SiO_2 shell had little impact on the heat generation/transfer for the physically mixed samples, resulting in a nearly identical decrease in PL signal intensity (Figures 3b and 3c), and consequently, temperature measurements (Figure S4). The similarities between these two samples confirm ballistic heat transfer through the thin SiO_2 shell layer and reaching the $YVO_4:Eu^{3+}$ phase. This method of transport allows for low-loss phonon diffusion to the particle surface, i.e., limited scattering of the phonons.

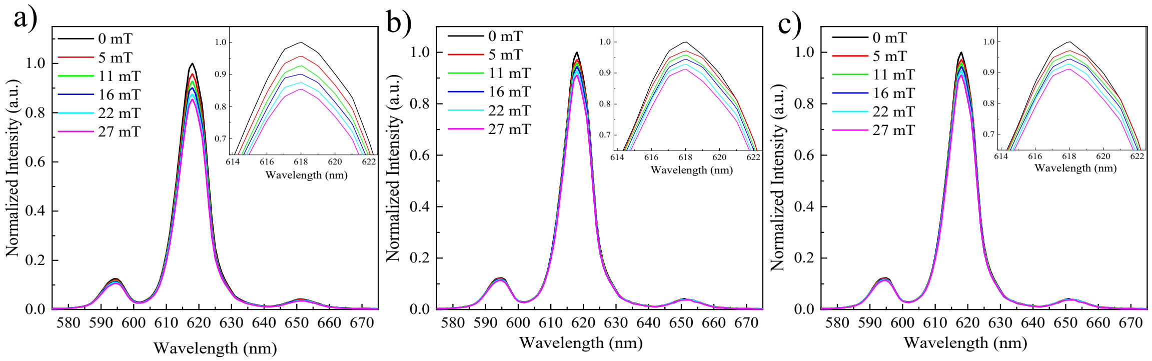

Figure 3: *in situ* PL spectra of $YVO_4:Eu^{3+}$ powders mixed with a) $Fe_3O_4|SiO_2$ at 2.51 wt ratio, b) $Fe_3O_4|SiO_2$ at 1.43 wt ratio, and c) Fe_3O_4 at 1.43 wt ratio. There are no major changes in PL signal intensity decrease between the Fe_3O_4 NPs with (b) and without (c) SiO_2 coating, demonstrating the remarkable sensitivity of the luminescent material as a temperature probe.

The localized temperatures can be directly extracted from the PL quenching after calibration of the temperature-dependent signal in an *in situ* heating stage (Figure 2d). Figure 4a shows a comparison between PL and fiber optic probe measurements for the physically mixed samples ($YVO_4:Eu^{3+}$-$Fe_3O_4|SiO_2$ mixtures). An apparent difference between the PL measurements and the fiber optic probe is seen, with differences up to 40 °C between the two techniques. Interestingly, the $YVO_4:Eu^{3+}$-Fe_3O_4 (without a SiO_2 shell) temperatures agree better for the PL and fiber optic probe, i.e., are within 18-27 °C, except at intermediate AMF intensities (from 11 mT to 22 mT, Figure 4b). These observations can be attributed to the reduced spatial resolution of fiber optic probes, which have a geometrical size much greater than the scale of heat transfer, positioning the probe at a distance where dissipation has already occurred. The presence of a poor thermally conducting SiO_2 shell slightly intensifies this effect, acting as a heat sink; however, for materials that are closer to the heat source, a temperature rise can still be detected. Physically mixing the temperature probe ($YVO_4:Eu^{3+}$) facilitates heat transfer and sensing at the nanoscale, which does not happen when using fiber optic probes. Furthermore, the temperature difference between 11 mT to 22 mT is attributed to heat dissipation losses (non-adiabatic) associated with the fiber optic experiment.[39] Truly adiabatic systems would exhibit a linear relationship between temperature and AMF.[41] The non-linear relationship between the AMF and observed temperature has been discussed by others[39, 41] and should exhibit a power-law response, as seen in Figure 4b.[6, 42-43] Because physical mixing facilitates ballistic heat transfer that is believed to occur at the NP scale[14-15, 20], fast heating rates are detected via the $YVO_4:Eu^{3+}$ PL when in contact with Fe_3O_4. Most treatments of heat dissipation due to magnetic hyperthermia are modeled with Fourier's Law and are measured with a fiber optic probe.[16] This model describes the macroscale (bulk) behavior correctly. However, this model does not account for nanoscale heating, causing cancer cell death[11] at ambient bulk temperatures. Unfortunately, it is complicated to model nanoscale heat transfer due to the complexities associated with phonon scattering.[14-15, 20, 25] As such, experimental studies considering heat dissipation at different scales are paramount to understanding local heating effects in AMFs. The PL probe method developed herein demonstrates an adiabatic response (the linear relationship), suggesting accurate temperature measurements.

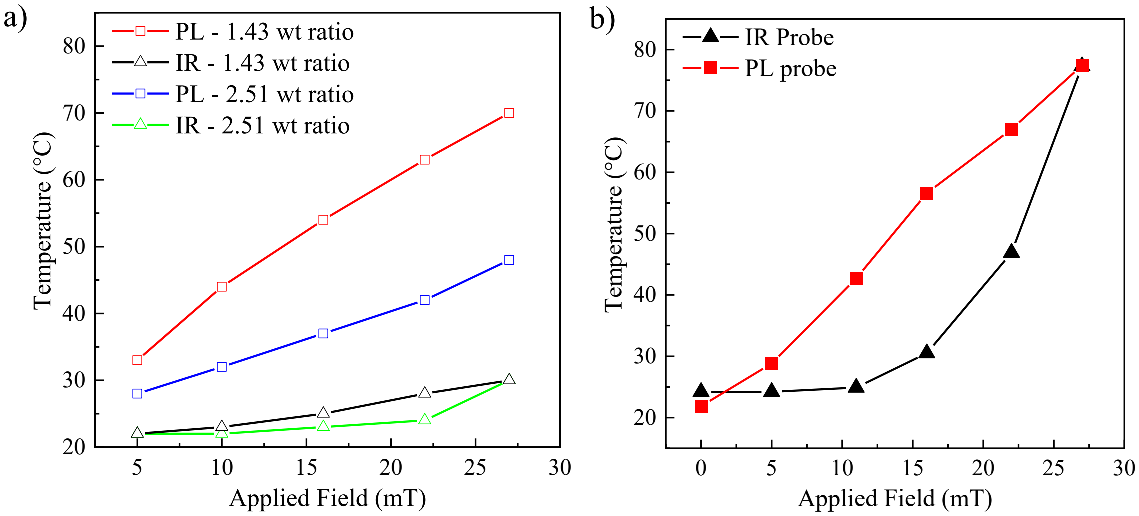

Figure 4: Extracted temperatures using PL (squares) and IR fiber optic (triangles) probes for $YVO_4:Eu^{3+}$ powders mixed with a) $Fe_3O_4|SiO_2$ at 2.51 wt ratio and 1.43 wt ratio, and b) uncoated Fe_3O_4 core at 1.43 wt ratio. When the SiO_2 coating is present, the fiber optic probe cannot detect temperatures higher than 30 °C, while the PL probe provides the same temperature reading at 1.43 wt regardless of the presence of SiO_2.

An explanation for the discrepancies between the two temperature measurements in Figure 4b was first introduced by Wang et al.[39] and Soetaert et al.[41] Specifically, as the AMF increases, temperature fluctuations are less significant and show better agreement between the fiber optics and PL. These thermal fluctuations are common at the onset of heating, for rates lower than 1 °C/s because of non-uniform temperature distribution and heat dissipation dominating the process.[39, 41] At heating rates higher than 1 °C/s (achieved for high fields 27 mT), thermal fluctuations are less significant (relative to the thermal gradient) resulting in the agreement between the fiber optic and PL measurements.[41] To demonstrate this experimentally, cooling studies were carried out by collecting the PL spectra with increasing delay times (30, 60, and 90s). Table 1 shows the calculated temperatures extracted from the time-delayed PL measurements for various applied fields. Temperature fluctuations at low fields (5 and 11 mT) do not follow a specific trend due to low heating rates. At higher fields (≥16 mT) the calculated temperature decrease increases with the time delay, i.e., more heat dissipation. Therefore, direct extrapolation of the temperature during under AMF was only possible for fields ≥16 mT. Based on these measurements, the heat dissipation occurring during a standard measurement (45 s) does not drastically impact the extrapolated temperatures (~10% deviation).

Table 1: Calculated temperatures extracted from a temperature dependent luminescent probe after various elapsed time from the moment the AMF is turned off. Small temperature variations are observed at low fields (< 11 mT) suggesting the rise in temperature may not be high enough to detect a cooling rate. Higher fields on the other hand, show a trend in decreasing temperature with time, consistent with cooling due to dissipation, enabling extrapolation of the temperature while the field was on.

	Cooling rate studies for a layered sample of $Fe_3O_4|SiO_2|YVO_4:Eu^{3+}$						
	Calculated Temperature (°C) Extracted from Luminescent Signal						
Delay times after field is turned off (s)	**5 mT**	**11 mT**	**16 mT**	**22 mT**	**27 mT**	**33 mT**	**37 mT**
0	32	41	50	58	65	69	73
30	33	44	49	57	57	63	65
60	36	42	49	54	58	59	61
90	36	40	48	52	57	58	58
Extrapolated Teperature for Field on (°C)	N/A	N/A	51	62	67	74	79

Next, the multi-layered $Fe_3O_4|SiO_2|YVO_4:Eu^{3+}$ sample was measured to directly probe the Fe_3O_4 surface temperature. As with the physically mixed samples, the PL intensity was calibrated up to 325 °C (Figure 5a). The normalized PL shows a linear decrease across the full temperature range (PL = 1.0408 - 0.00276 T(°C)). Based on the calibration studies, the relative PL sensitivity is 0.003 °C^{-1}, as defined from by $(\Delta I/\Delta T) * (1/\Delta I)$.[37] The multi-layerd sample exhibits a 27% decrease in intensity 27 mT (Figure 5b), 11% larger than the physically mixed sample (Table S1). The extracted temperatures are assumed to be the Fe_3O_4 surface temperature since no heat loss is expected in the SiO_2 due to ballistic transport. Table 2 shows the calculated temperature values extracted from the *in situ* experiment shown in Figure 5b, constantly estimating values at least 25 °C higher than the fiber optic measurements at low AMFs. However, significantly higher temperatures differences (64 °C) are extracted at larger AMFs, than previously reported[26, 37],

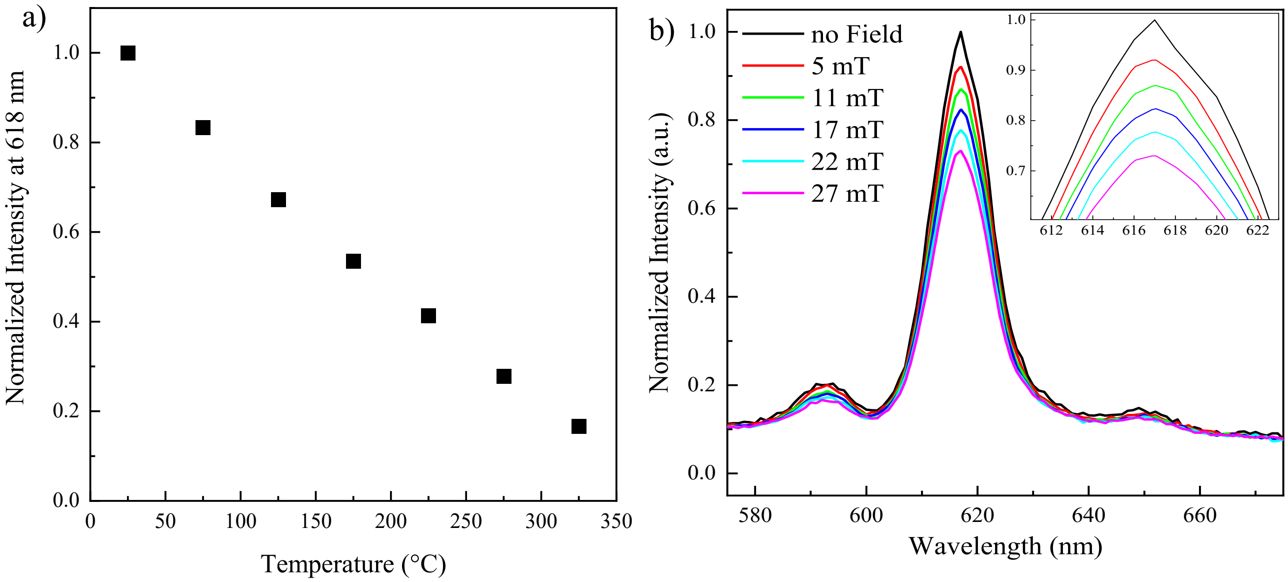

Figure 5: a) Correlation between PL intensity and temperature spectra for a layered sample where $Fe_3O_4|SiO_2$ is in close proximity (5.5 nm) to the $YVO_4:Eu^{3+}$ NPs performed on the Linkham temperature stage, and b) under increasing AMFs. The decrease in luminescent intensity with applied field is more pronounced than in physically mixed samples and pure $YVO_4:Eu^{3+}$.

Table 2: Calculated temperatures extracted from a temperature dependence luminescent probe near the NP surface compared to a bulk measurement. The differences in temperature show how heat dissipation is ballistic at the nanoscale, creating a temperature gradient around the NP.

	Extracted from Fiber Optic Probe		Extracted from PL	
Applied Field (mT)	Measured Bulk Temperature (Fe_3O_4)	Measured Bulk Temperature ($Fe_3O_4|SiO_2|YVO_4:Eu^{3+}$)	Calculated Temperature (°C)	Difference
5	25	23	48 ± 18	25
11	27	28	71 ± 20	43
16	34	41	98 ± 11	57
22	52	64	127 ± 13	63
27	89	90	154 ± 7	64

demonstrating the importance of close contact between the heat source and the thermal probe. Interestingly, the standard deviation (7 °C) at the highest AMF (27 mT) is of the same order of magnitude as the temperature difference extrapolated from the cooling studies to account for the 45 s of data collection (6 °C, Table 1), emphasizing no temporal resolution losses.

To highlight the importance of contact between the particle multi-layers, a second sample was measured with poor contact between the $YVO_4:Eu^{3+}$ and SiO_2 layers caused by delamination (Figure S5). This system was expected to exhibit more heat dissipation and lower overall temperatures than the multi-layered sample with good contact but better than the physically mixed samples. For this sample, the estimated temperatures (shown as blue squares in Figure 6) are lower than the homogeneously layered sample (green squares). Moreover, physically mixed samples measured with PL (red squares) result in lower temperature measurements than the two layered samples, systematically demonstrating lower sensitivity to temperature increases proportional to the Fe_3O_4-$YVO_4:Eu^{3+}$ separation distances. In contrast, fiber optic measurements consistently estimated lower temperatures for physically mixed (pink triangles) and multi-layered (black triangles) samples. Because this work performed all measurements in bulk powders, higher temperature differences are observed when compared to other thermal sensing experiments in aqueous media.[13, 37] It is believed that the temperature discrepancies will be significnatly larger for NP suspensions due to lower particle densities and diffusion reducing the contact Fe_3O_4-$YVO_4:Eu^{3+}$ contact.

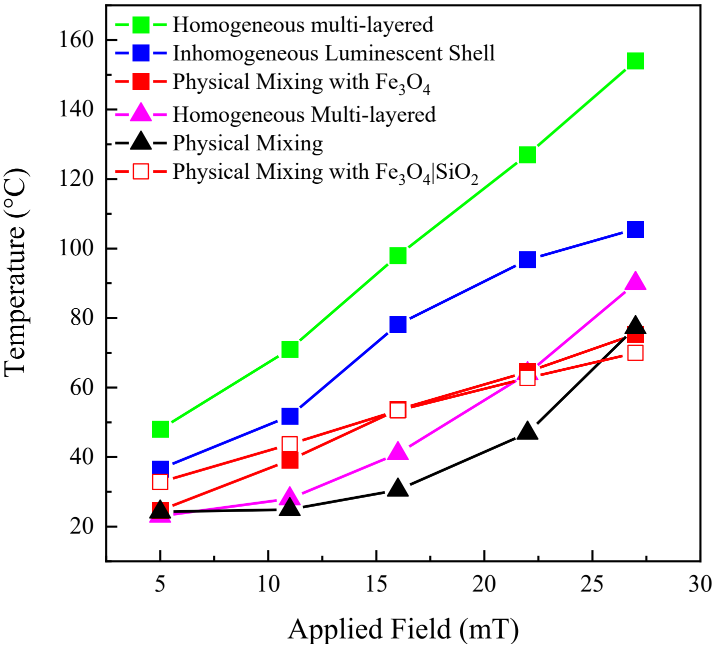

Figure 6: Summary of all temperature measurements obtained at different distances from the heating core, and extracted via PL sensing and fiber-optic probes. As the PL material gets closer to the heat source, greater thermal differences between fiber optic and PL probe are observed.

However, the aqueous phase comparison is beyond the scope of this work. Therefore, there is a crucial improvement in spatial resolution by having the luminescent probe in close contact with the Fe_3O_4 phase. Arguabily, the concept of spatial resolution is somewhat elusive in the ballistic heat transfer regime, because a 5.5 nm SiO_2 spacer layer did not affect temperature readings significantly when using the PL probe, indicating the observed temperature is likely the surface temperature. In contrast, at the bulk level (fiber optic probe) significantly lower temperatures were observed, indicating heat dissipation dictates spatial resolution. Furthermore, for the $Fe_3O_4|SiO_2$ sample with $YVO_4:Eu^{3+}$ deposited homogeneously, measurement uncertainty is reduced due to the normalization of the average distance between each $Fe_3O_4|SiO_2$ and $YVO_4:Eu^{3+}$ pair. Lastly, in terms of expanding such probing experiment to other NP structures and compositions, this method is limited by the ability to deposit luminescent shells around Fe_3O_4 NPs of octahedral, cubic, nanodisk shapes and exchange-couple nanomaterials without oxidation of the core.[19] Since these structures have a substantial contribution to the effective anisotropy,[22] and distinct contribution to heating due to their spin structures, the magnitude of heat dissipation changes[44], which means they would need to be studied individually to extend this method to other magnetic NPs. Nonetheless, exposing the differences in thermal measurements imapact biological and catalytic applications significantly, because cell death or coking can happen without measurable bulk temperature changes due to incorrect temperatures unbeknownst to researchers, emphasizing the need for nanoscale probes, and providing a future route to a more generalized method for comparing the efficiency of magnetic NP heating.

CONCLUSION

The temporal and spatial resolution of temperature measurements near magnetic Fe_3O_4 NPs during the application of high AMFs has shown to be an obstacle for advancements in induction heating applications. This work demonstrated the successful fabrication of a multi-layered $Fe_3O_4|SiO_2|YVO_4:Eu^{3+}$ system for direct probing of the temperature via luminescence sensing. Such nanostructure design improved spatial resolution to a maximum of 5.5 nm from the NP surface and reduced quenching without compromising sensitivity by introducing a spacer layer. A 64 °C difference at 27 mT was detected between the environment near the NP and bulk media, unveiling the presence of a thermal gradient that can affect applications with induction heating. Furthermore, the signal-to-noise ratio increased by 1.6x, yielding higher temperature sensitivity. Another sensitivity improvement was observed for physical mixing of $YVO_4:Eu^{3+}$ and Fe_3O_4, resulting in enhanced detection of temperature rise compared to a fiber optic probe measurement due to facilitated heat transfer at the nanoscale (physical mixing) though not as sensitive as the multi-layered sample. Moreover, the standard deviation on the temperature values at higher AMFs are of the same order of magnitude of the sample cooling effect at times greater than the time elapsed for PL spectra collection, showing these experiments were not negatively affected by temporal resolution. Therefore, this work has a significant contribution to the applications of magnetic NPs in induction heating, allowing high temperature detection not possible with organic molecules, required for catalytic applications, with the multi-layered sample design without the thermal degradation of the molecular probe, offering accurate temperature determination without compromising luminescent signal intensity.

Methods

Chemicals

1-octadecene (90% technical grade), dibenzyl ether (98%), Citric Acid Anhydrous (99.5%) oleic acid (90% technical grade), yttrium(III) nitrate hexahydrate (99.9% REO), europium(III) nitrate hydrate (99.99% REO), and ammonium vanadium oxide (99.0% ACS) were purchased from Alfa Aesar. Acetone (99.5%), ammonium hydroxide (28-30%, ACS grade), cyclohexane (99%), methanol (99.8% ACS grade), toluene (99.5%), and reagent alcohol (94-96%, ACS grade ethanol + methanol) were purchased from VWR. Iron (III) anhydrous (>98%, Merck), sodium oleate (NaOL) (> 97.0%, TCI), Igepal CO-520 (Spectrum Chemical), tetraethyl orthosilicate (99%, Sigma-Aldrich). All reagents were used without further purification.

Synthesis of Fe_3O_4 cores

Magnetic Fe_3O_4 nanospheres were synthesized via thermal decomposition route as described elsewhere.[45] Briefly, an iron oleate (FeOL) complex was prepared by reacting 15 mmol of $FeCl_3$ with 45 mmol of NaOL in a solution containing hexane, water, and ethanol at 2:1:1 ratio (200 mL total volume). The solution was then brought to reflux (~56 °C) for 1 hr under a nitrogen atmosphere. After the reaction, the FeOL is formed in the hexane layer, and therefore it is separated from the aqueous layer via a separatory funnel. The hexane layer is washed several times with DI water until no Cl^- ions are detected via a simple $Ag(NO_3)$ test. The hexane layer is collected and dried at 110 °C under vigorous stirring overnight. For optimum morphological control, it is recommended to use distilled and DI water to reduce the possibility of impurities in the FeOL precursor. Lastly, the FeOL is thermally decomposed in a three-neck round bottom flask, with oleic acid (OA), 1-octadecene (ODE) and di-benzyl ether (BE). The amount of oleic acid used varied according to the desired NP diameter, namely 13 mmol for 28 nm. The ratio of ODE:BE used was 2:1 (15 mL total volume). The solution was degassed at 90 °C for 30 min, then under inert atmosphere brought to 200 °C, and a heating ramp of 3.3 °C/min is implemented from 200-325 °C. The solution is aged for 30 min under reflux, and the particles are collected by centrifuging the products in toluene:acetone (1:3 vol) at least five times. The particles are then re-suspended in methanol and dried under vacuum at 110 °C. Excess methanol is removed with a magnet to shorten drying time to 1 hr and reduce NP oxidation.

SiO_2 shell deposition

The SiO_2 shell deposition is performed via reverse microemulsion to allow NP phase transfer and subsequent shell deposition**.** This process has been described elsewhere**.**[46] Once the Fe_3O_4 core particles have been dried; they are grinded, dispersed in cyclohexane at a 1.25 mg/mL concentration, and sonicated for 20 min. In a separate 20-mL vial, 0.50g of IGEPAL CO-520 is mixed with 11 mL of cyclohexane and sonicated for 10 min. Afterwards, under vigorous stirring, 2 mL of the Fe_3O_4 solution are added to the 20-mL vial. Subsequently, 50 µL of ammonium hydroxide are added, followed by 20 µL of TEOS, and the solution is stirred for 16 hrs. The $Fe_3O_4|SiO_2$ NPs are collected by centrifugation with toluene:ethanol (1:4 v/v) three times. Prior to the luminescent shell deposition, the NPs are dried under vacuum and annealed at 450 °C under Ar/H_2 (95%/5%) for 2 hr to allow for densification of the SiO_2 shell without oxidation of the Fe_3O_4 core.

$YVO_4:Eu^{3+}$ (5 mol%) shell deposition

After densification of the SiO_2 shell, the amounts of precursors needed for the $YVO_4:Eu^{3+}$ deposition were calculated based on the average core-shell diameter of the $Fe_3O_4|SiO_2$ NPs. This method for luminescent shell deposition has been demonstrated successfully by our group in other works.[27, 30] For a 10 nm shell deposition, 12.3g of citric acid were dissolved in 15.6 mL of DI water and briefly sonicated to dissolve the citric acid. Then, 26 mg of the core-shell NPs were added to this solution under vigorous stirring. Subsequently, 45.3 mmol of $Y(NO_3)_3.6H_2O$ (174 mg), 2.38 mmol of $Eu(NO_3)_3.6H_2O$ (8.1 mg) and 45.3 mmol of NH_4VO_3 (53 mg) were added to the mixture in a water bath set to 40-50 °C, and the pH was adjusted to 9. The resultant solution was washed with water and ethanol several times and dried under vacuum at 100 °C. The amorphous powders were annealed at 300 °C for 45 min to remove the citric acid binder, solidify the shell, and prevent sintering of the NPs.

Structural and Optical Characterization

The core-shell-shell NPs were characterized via X-ray diffraction (XRD) using a PANalytical X-ray diffractometer, operating at 45 kV and 40 mA, with a Cu Kα1 ($\alpha = 1.54$ Å) as a radiation source. The $\theta-2\theta$ radial scan was performed over the range 20−70° with a step size of 0.04° and a dwell time of 60 s. The NP size and shape were characterized by transmission electron microscopy (TEM) using a JEOL JEM-1400 operating at 120 kV, and using an Orius Camera SC1000A 1, with a 0.20 nm lattice image resolution and 0.38 nm point image resolution. For lattice fringe and crystal phase identification, JEOL JEM-2011 TEM was used, operating at 200 kV and using a CCD camera with a 0.14 nm lattice resolution. The YVO_4:Fe_3O_4 ratio was measured using a PerkinElmer Optima 8000 ICP-OES spectrometer and calibrated to commerical Y and Fe standards (VWR).

The in situ PL spectra were measured using an Edinburgh Instruments FLS1000 PL spectrometer equipped with a PMT detector and a 450 W ozone-free xenon arc lamp as the light source. Excitation and emission scans were collected with a 4 nm bandpass at a scan rate of 0.4 nm $s^{-}1$ in the range of 240–400 nm (excitation) and 575–675 nm (emission) with 1 nm step size. The powder samples were placed onto a quartz sample holder for PL measurements. Physically mixing of Fe_3O_4 and YVO_4:Eu^{3+} powders were done based on the weight of the core Fe_3O_4 (without SiO_2) and YVO_4 powders. The mass of the SiO_2 layer was estimated, assuming a conformal 5 nm shell layer. The calibration temperature measurements were taken in a LINKAM THMS600 temperature-controlled stage using $YVO_4:Eu^{3+}$ NPs in a quartz dish, at every 50 °C from 25°C to 325 °C for every sample before applied magnetic field analysis. For this experiment, surface temperature and stage temperature are assumed to be equivalent since the thermal stage was equilibrated for 5 min before each measurement. The data was linearly fitted and used for temperature calculation under AMFs. For the *in situ* magnetic field-temperature-dependent PL measurements, an in-house setup was accomplished by using the same fiber optic cables from the LINKAM THMS600 temperature-controlled stage and a 3-turn coil, 1 in diameter, with variable current (0-600 A) Ambrell EASYHEAT 8130LI 10 kW induction heater, at a constant frequency of 343 kHz (Figure S6). The sample is heated for 2 min via induction, which is when a constant temperature reading was observed with a fiber optic probe. The PL spectra is collected immediately after so that the heating induced by the magnetic field can be converted to temperature when comparing both experiments. Because the magnetic field can interfere with the functioning of the PL spectrophotometer, causing energy level splitting, inhibiting the collection of a clear PL spectrum, and possibly damaging the metallic components of the instrument, a simultaneous measurement is not possible. However, the data is collected immediately after within a 45 s time span. Because the objective of this work is to observe a reduction in PL intensity due to heating and not the effect of the magnetic field, not performing the PL measurement while the field is on does not interfere with temperature probing, aside from heat dissipation considerations (discussed above). Alternatively, experiments with various cooling times 0, 30, 60, and 90s were performed to extrapolate the temperature, accounting for the cooling that occurs during the PL spectra collection (~ 45 s).

The fiber optic tubes were placed at maximum proximity to the coil before induction heating was observed on the tubes themselves. The fiber optic photoluminescence tubes were monitored with a fiber optic temperature probe (Qualitrol) to avoid damaging the equipment while the magnetic field was activated. The sample was placed in a quartz powder holder at the center of the coil, and the whole setup was covered to avoid interference from external light. For the bulk temperature changes under an alternating magnetic field, the sample was placed in a capillary tube and centered inside the same induction heating system. The fiber optic probed was placed directly on top of the NPs, and temperature profiles were collected for the same amount of time (2 min). The field was then turned off, and cooling rates were collected.

ASSOCIATED CONTENT

Supporting Information. The following files are available free of charge.

Supplementary characterization (PDF)

AUTHOR INFORMATION

Corresponding Author

*James Dorman – jamesdorman@lsu.edu

Author Contributions

The manuscript was written through contributions of all authors. All authors have given approval to the final version of the manuscript.

ACKNOWLEDGMENT

N.S.M. acknowledges the fellowship support from the Louisiana College of Engineering, the Chevron Fellowship Award, and the U.S. Department of Energy (DOE) under EPSCOR grant no. DE-SC0012432. K.R.B. acknowledges the Louisiana Board of Regents (LEQSF(2016–19)-RD-A-03) for financial support. J.A.D.and K.M.D would also like to acknowledge the National Science Foundation, Chemical, Biological, Environmental, and Transport systems for funding under grant no. 1805785.

REFERENCES

1. Mortensen, P. M.; Engbæk, J. S.; Vendelbo, S. B.; Hansen, M. F.; Østberg, M., Direct Hysteresis Heating of Catalytically Active Ni–Co Nanoparticles as Steam Reforming Catalyst. *Industrial & Engineering Chemistry Research* **2017**, *56*, 14006-14013.
2. Meffre, A.; Mehdaoui, B.; Connord, V.; Carrey, J.; Fazzini, P. F.; Lachaize, S.; Respaud, M.; Chaudret, B., Complex Nano-Objects Displaying Both Magnetic and Catalytic Properties: A Proof of Concept for Magnetically Induced Heterogeneous Catalysis. *Nano Letters* **2015**, *15*, 3241-3248.
3. Wang, W.; Tuci, G.; Duong-Viet, C.; Liu, Y.; Rossin, A.; Luconi, L.; Nhut, J.-M.; Nguyen-Dinh, L.; Pham-Huu, C.; Giambastiani, G., Induction Heating: An Enabling Technology for the Heat Management in Catalytic Processes. *ACS Catalysis* **2019**, *9*, 7921-7935.
4. Giambastiani, G.; Wang, W.; Duong-Viet, C.; Tuci, G.; Liu, Y.; Rossin, A.; Luconi, L.; Nhut, J.-M.; Nguyen-Dinh, L.; Pham-Huu, C., Highly Nickel-Loaded Γ-Alumina Composites for a Radiofrequency-Heated, Low-Temperature CO_2 Methanation Scheme. *ChemSusChem*, **2020**, 13, 5341.
5. Whajah, B.; da Silva Moura, N.; Blanchard, J.; Wicker, S.; Gandar, K.; Dorman, J. A.; Dooley, K. M., Catalytic Depolymerization of Waste Polyolefins by Induction Heating: Selective Alkane/Alkene Production. *Industrial & Engineering Chemistry Research* **2021**, *60*, 15141-15150.
6. Riedinger, A.; Guardia, P.; Curcio, A.; Garcia, M. A.; Cingolani, R.; Manna, L.; Pellegrino, T., Subnanometer Local Temperature Probing and Remotely Controlled Drug Release Based on Azo-Functionalized Iron Oxide Nanoparticles. *Nano Letters* **2013**, *13*, 2399-2406.
7. Mohammadi Ziarani, G.; Malmir, M.; Lashgari, N.; Badiei, A., The Role of Hollow Magnetic Nanoparticles in Drug Delivery. *RSC Advances* **2019**, *9*, 25094-25106.
8. Espinosa, A.; Di Corato, R.; Kolosnjaj-Tabi, J.; Flaud, P.; Pellegrino, T.; Wilhelm, C., Duality of Iron Oxide Nanoparticles in Cancer Therapy: Amplification of Heating Efficiency by Magnetic Hyperthermia and Photothermal Bimodal Treatment. *ACS Nano* **2016**, *10*, 2436-2446.
9. Nemati, Z.; Alonso, J.; Martinez, L. M.; Khurshid, H.; Garaio, E.; Garcia, J. A.; Phan, M. H.; Srikanth, H., Enhanced Magnetic Hyperthermia in Iron Oxide Nano-Octopods: Size and Anisotropy Effects. *The Journal of Physical Chemistry C* **2016**, *120*, 8370-8379.
10. Nguyen, H.; Ohannesian, N.; Bandara, P. C.; Ansari, A.; Deleo, C. T.; Rodrigues, D.; Martirosyan, K. S.; Shih, W.-C., Magnetic Active Water Filter Membrane for Induced Heating to Remove Biofoulants. *ACS Applied Materials & Interfaces* **2020**, *12*, 10291-10298.
11. Creixell, M.; Bohórquez, A. C.; Torres-Lugo, M.; Rinaldi, C., Egfr-Targeted Magnetic Nanoparticle Heaters Kill Cancer Cells without a Perceptible Temperature Rise. *ACS Nano* **2011**, *5*, 7124-7129.

12. Lisk, P.; Bonnot, E.; Rahman, M. T.; Pollard, R.; Bowman, R.; Degirmenci, V.; Rebrov, E. V., Magnetic Actuation of Catalytic Microparticles for the Enhancement of Mass Transfer Rate in a Flow Reactor. *Chemical Engineering Journal* **2016**, *306*, 352-361.
13. Piñol, R., et al., Joining Time-Resolved Thermometry and Magnetic-Induced Heating in a Single Nanoparticle Unveils Intriguing Thermal Properties. *ACS Nano* **2015**, *9*, 3134-3142.
14. Cahill, D. G.; Ford, W. K.; Goodson, K. E.; Mahan, G. D.; Majumdar, A.; Maris, H. J.; Merlin, R.; Phillpot, S. R., Nanoscale Thermal Transport. *Journal of Applied Physics* **2003**, *93*, 793-818.
15. Cahill, D. G., et al., Nanoscale Thermal Transport. Ii. 2003–2012. *Applied Physics Reviews* **2014**, *1*, 011305.
16. Chen, B. C.; Ho, C. Y.; Kao, L. J.; Wu, W. C.; Tsai, Y. H.; Ma, C., Hysteresis Loss-Induced Temperature in Ferromagnetic Nanoparticle. *IEEE Transactions on Magnetics* **2014**, *50*, 1-4.
17. Dennis, C. L.; Ivkov, R., Physics of Heat Generation Using Magnetic Nanoparticles for Hyperthermia. *International Journal of Hyperthermia* **2013**, *29*, 715-729.
18. Tong, S.; Quinto, C. A.; Zhang, L.; Mohindra, P.; Bao, G., Size-Dependent Heating of Magnetic Iron Oxide Nanoparticles. *ACS Nano* **2017**, *11*, 6808-6816.
19. Robles, J.; Das, R.; Glassell, M.; Phan, M. H.; Srikanth, H., Exchange-Coupled $Fe_3O_4/CoFe_2O_4$ Nanoparticles for Advanced Magnetic Hyperthermia. *AIP Advances* **2018**, *8*, 056719.
20. Joshi, A. A.; Majumdar, A., Transient Ballistic and Diffusive Phonon Heat Transport in Thin Films. *Journal of Applied Physics* **1993**, *74*, 31-39.
21. Bakoglidis, K. D.; Simeonidis, K.; Sakellari, D.; Stefanou, G.; Angelakeris, M., Size-Dependent Mechanisms in Ac Magnetic Hyperthermia Response of Iron-Oxide Nanoparticles. *IEEE Transactions on Magnetics* **2012**, *48*, 1320-1323.
22. Lavorato, G. C.; Das, R.; Xing, Y.; Robles, J.; Litterst, F. J.; Baggio-Saitovitch, E.; Phan, M.-H.; Srikanth, H., Origin and Shell-Driven Optimization of the Heating Power in Core/Shell Bimagnetic Nanoparticles. *ACS Applied Nano Materials* **2020**, *3*, 1755-1765.
23. Nemati, Z.; Salili, S. M.; Alonso, J.; Ataie, A.; Das, R.; Phan, M. H.; Srikanth, H., Superparamagnetic Iron Oxide Nanodiscs for Hyperthermia Therapy: Does Size Matter? *Journal of Alloys and Compounds* **2017**, *714*, 709-714.
24. Wells, J., et al., Challenges and Recommendations for Magnetic Hyperthermia Characterization Measurements. *International Journal of Hyperthermia* **2021**, *38*, 447-460.
25. Kaiser, J.; Feng, T.; Maassen, J.; Wang, X.; Ruan, X.; Lundstrom, M., Thermal Transport at the Nanoscale: A Fourier's Law Vs. Phonon Boltzmann Equation Study. *Journal of Applied Physics* **2017**, *121*, 044302.
26. Dong, J.; Zink, J. I., Taking the Temperature of the Interiors of Magnetically Heated Nanoparticles. *ACS Nano* **2014**, *8*, 5199-5207.
27. Dorman, J. A.; Choi, J. H.; Kuzmanich, G.; Chang, J. P., High-Quality White Light Using Core–Shell $RE^{3+}:LaPO_4$ (RE = Eu, Tb, Dy, Ce) Phosphors. *The Journal of Physical Chemistry C* **2012**, *116*, 12854-12860.
28. Brites, C. D. S.; Lima, P. P.; Silva, N. J. O.; Millán, A.; Amaral, V. S.; Palacio, F.; Carlos, L. D., Thermometry at the Nanoscale. *Nanoscale* **2012**, *4*, 4799-4829.
29. Getz, M. N.; Nilsen, O.; Hansen, P.-A., Sensors for Optical Thermometry Based on Luminescence from Layered YVO_4: Ln^{3+} (Ln = Nd, Sm, Eu, Dy, Ho, Er, Tm, Yb) Thin Films Made by Atomic Layer Deposition. *Scientific Reports* **2019**, *9*, 10247.

30. R Bajgiran, K.; Darapaneni, P.; Melvin, A. T.; Dorman, J. A., Effects of Weak Electric Field on the Photoluminescence Behavior of Bi^{3+}-Doped $YVO_4:Eu^{3+}$ Core–Shell Nanoparticles. *The Journal of Physical Chemistry C* **2019**, *123*, 13027-13035.

31. Riwotzki, K.; Haase, M., Wet-Chemical Synthesis of Doped Colloidal Nanoparticles: YVO_4:Ln (Ln = Eu, Sm, Dy). *The Journal of Physical Chemistry B* **1998**, *102*, 10129-10135.

32. Tong, L.; Shi, J.; Liu, D.; Li, Q.; Ren, X.; Yang, H., Luminescent and Magnetic Properties of $Fe_3O_4@SiO_2@Y_2O_3:Eu^{3+}$ Composites with Core–Shell Structure. *The Journal of Physical Chemistry C* **2012**, *116*, 7153-7157.

33. Das, A.; Mohanty, S.; Kumar, R.; Kuanr, B. K., Tailoring the Design of a Lanthanide Complex/Magnetic Ferrite Nanocomposite for Efficient Photoluminescence and Magnetic Hyperthermia Performance. *ACS Applied Materials & Interfaces* **2020**, *12*, 42016-42029.

34. Moura, N. S.; Bajgiran, K. R.; Roman, C. L.; Daemen, L.; Cheng, Y.; Lawrence, J.; Melvin, A. T.; Dooley, K. M.; Dorman, J. A., Catalytic Enhancement of Inductively Heated Fe_3O_4 Nanoparticles by Removal of Surface Ligands. *ChemSusChem* **2021**, *14*, 1122-1130.

35. Tang, J.; Myers, M.; Bosnick, K. A.; Brus, L. E., Magnetite Fe_3O_4 Nanocrystals: Spectroscopic Observation of Aqueous Oxidation Kinetics. *The Journal of Physical Chemistry B* **2003**, *107*, 7501-7506.

36. Zaoui, H.; Palla, P. L.; Cleri, F.; Lampin, E., Length Dependence of Thermal Conductivity by Approach-to-Equilibrium Molecular Dynamics. *Physical Review B* **2016**, *94*, 054304.

37. Lin, X.; Kong, M.; Wu, N.; Gu, Y.; Qiu, X.; Chen, X.; Li, Z.; Feng, W.; Li, F., Measurement of Temperature Distribution at the Nanoscale with Luminescent Probes Based on Lanthanide Nanoparticles and Quantum Dots. *ACS Applied Materials & Interfaces* **2020**, *12*, 52393-52401.

38. Wang, S.; Westcott, S.; Chen, W., Nanoparticle Luminescence Thermometry. *The Journal of Physical Chemistry B* **2002**, *106*, 11203-11209.

39. Wang, S.; Huang, S.; Borca-Tasciuc, D., Potential Sources of Errors in Measuring and Evaluating the Specific Loss Power of Magnetic Nanoparticles in an Alternating Magnetic Field. *IEEE Transactions on Magnetics* **2013**, *49*, 255-262.

40. Du, G.; Liu, P.; Guo, W.; Han, Y.; Zhang, J.; Ma, Z.; Han, J.; Liu, Z.; Yao, K., The Influence of High Magnetic Field on Electric-Dipole Emission Spectra of Eu^{3+} in Different Single Crystals. *Journal of Materials Chemistry C* **2013**, *1*, 7608-7613.

41. Soetaert, F.; Kandala, S. K.; Bakuzis, A.; Ivkov, R., Experimental Estimation and Analysis of Variance of the Measured Loss Power of Magnetic Nanoparticles. *Scientific Reports* **2017**, *7*, 6661.

42. Rosensweig, R. E., Heating Magnetic Fluid with Alternating Magnetic Field. *Journal of Magnetism and Magnetic Materials* **2002**, *252*, 370-374.

43. Makridis, A.; Curto, S.; Van Rhoon, G.; Samaras, T.; Angelakeris, M., A Standardisation Protocol for Accurate Evaluation of Specific Loss Power in Magnetic Hyperthermia. *Journal of Physics D: Applied Physics* **2019**, *52*, 255001.

44. Das, R.; Rinaldi-Montes, N.; Alonso, J.; Amghouz, Z.; Garaio, E.; García, J. A.; Gorria, P.; Blanco, J. A.; Phan, M. H.; Srikanth, H., Boosted Hyperthermia Therapy by Combined Ac Magnetic and Photothermal Exposures in Ag/Fe_3O_4 Nanoflowers. *ACS Applied Materials & Interfaces* **2016**, *8*, 25162-25169.

45. Chen, R.; Christiansen, M. G.; Sourakov, A.; Mohr, A.; Matsumoto, Y.; Okada, S.; Jasanoff, A.; Anikeeva, P., High-Performance Ferrite Nanoparticles through Nonaqueous Redox Phase Tuning. *Nano Letters* **2016**, *16*, 1345-1351.
46. Ding, H. L.; Zhang, Y. X.; Wang, S.; Xu, J. M.; Xu, S. C.; Li, G. H., Fe_3O_4@SiO_2 Core/Shell Nanoparticles: The Silica Coating Regulations with a Single Core for Different Core Sizes and Shell Thicknesses. *Chemistry of Materials* **2012**, *24*, 4572-4580.

TOC Figure

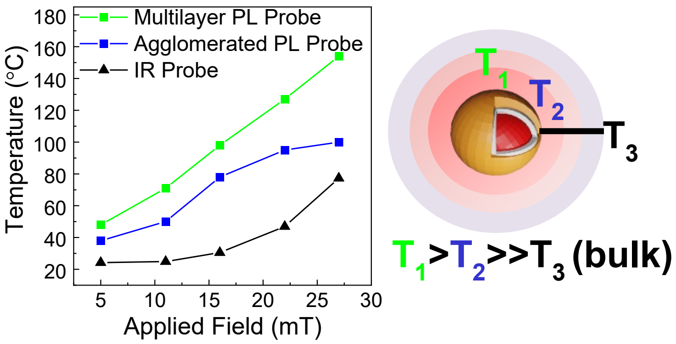

Multilayer PL Probe
Agglomerated PL Probe
IR Probe
Temperature (°C)
180
160
140
120
100
80
60
40
20
5
10
15
20
25
30
Applied Field (mT)
T_1
T_2
T_3
$T_1 > T_2 >> T_3$ (bulk)